Superconducting 2D NbS$_2$ Grown Epitaxially by Chemical Vapor Deposition

Zhenyu Wang,[⊥] Cheol-Yeon Cheon,[⊥] Mukesh Tripathi, Guilherme Migliato Marega, Yanfei Zhao, Hyun Goo Ji, Michal Macha, Aleksandra Radenovic, and Andras Kis*

Read Online

ACCESS | 📊 Metrics & More | 📖 Article Recommendations | 🆂🅸 Supporting Information

ABSTRACT: Metallic two-dimensional (2D) transition metal dichalcogenides (TMDCs) are attracting great attention because of their interesting low-temperature properties such as superconductivity, magnetism, and charge density waves (CDW). However, further studies and practical applications are being slowed down by difficulties in synthesizing high-quality materials with a large grain size and well-determined thickness. In this work, we demonstrate epitaxial chemical vapor deposition (CVD) growth of 2D NbS$_2$ crystals on a sapphire substrate, with a thickness-dependent structural phase transition. NbS$_2$ crystals are epitaxially aligned by the underlying c-plane sapphire resulting in high-quality growth. The thickness of NbS$_2$ is well controlled by growth parameters to be between 1.5 and 10 nm with a large grain size of up to 500 μm. As the thickness increases, we observe in our NbS$_2$ a transition from a metallic 3R-polytype to a superconducting 2H-polytype, confirmed by Raman spectroscopy, aberration-corrected scanning transmission electron microscopy (STEM) and electrical transport measurements. A Berezinskii−Kosterlitz−Thouless (BKT) superconducting transition occurs in the CVD-grown 2H-phase NbS$_2$ below the transition temperature (T_c) of 3 K. Our work demonstrates thickness and phase-controllable synthesis of high-quality superconducting 2D NbS$_2$, which is imperative for its practical applications in next-generation TMDC-based electrical devices.

KEYWORDS: two-dimensional superconductors, phase transition, CVD, transition metal dichalcogenides, niobium disulfide
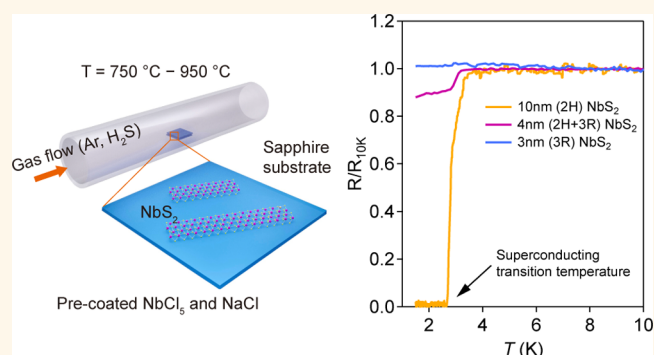
INTRODUCTION

Semiconducting two-dimensional (2D) transition metal dichalcogenides (TMDCs) have been heavily studied because of their layer-number-dependent bandgap[1] and outstanding performance as field-effect transistors[2] and optoelectronic devices.[3] In contrast to semiconducting TMDCs, metallic TMDCs (e.g., NbS$_2$, NbSe$_2$) are attracting great attention in the context of realizing 2D metal−semiconductor junctions with semiconducting TMDCs[4,5] with the aim of lowering contact resistance by weakening Fermi level pinning.[6] They are expected to be ideal 2D metal electrodes thanks to their van der Waals (vdW) interaction and small lattice mismatch with other TMDCs,[7] enhancing electrical performance compared with conventional 3D metal electrodes. Additionally, these metallic TMDCs hold interesting low-temperature properties such as superconductivity,[8,9] magnetism,[10] and charge density waves[11,12] (CDW), where superconducting TMDCs could be used to observe Andreev reflection in 2D systems[13,14] and realize Josephson junctions.[15] Among metallic TMDCs, 2H-NbS$_2$ is a peculiar case in that it is the only superconductor with no CDW instabilities observed experimentally.[8] This is unusual if

compared with other isostructural and isoelectronic compounds such as 2H-NbSe$_2$ and 2H-TaS$_2$, where superconductivity coexists with CDW order. Theoretical work, however, points out that 2H-NbS$_2$ is on the verge of CDW order in the 2D limit[16] or even close to spin density wave instabilities[17] possibly induced by magnetic impurities.[18] This makes 2D NbS$_2$ an appealing material platform to explore quantum phase transition. These interesting electronic properties and its potential device applications motivate the development of methods to synthesize 2D metallic and superconducting NbS$_2$.

Niobium disulfide (NbS$_2$) mainly exists in two polytypes: rhombohedral (3R) and hexagonal (2H), which exhibit distinct electrical properties. In 3R-NbS$_2$, metallicity has been confirmed
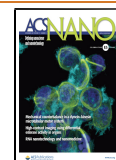
with a minimum resistance at around 30 K.[19] On the other hand, superconductivity can be observed in bulk 2H-NbS$_2$ below the transition temperature (T_c) of 6 K.[8] These two phases can be selectively grown in bulk by changing the sulfur pressure,[20] whereas reports on control over the polytypes in the few-layer limit are rare. Although 2D NbS$_2$ can be obtained by mechanical exfoliation from bulk crystals,[21,22] the flakes are usually several μm in size with little control over the thickness. In recent years, several attempts for growing NbS$_2$ using CVD have been reported.[19,23,24] Nevertheless, only 3R-phase metallic NbS$_2$ has been grown, with a limited domain size and lack of precise layer number control. Growing large-grain and superconducting 2H-phase NbS$_2$ with controllable thickness has not been reported yet, hindering the exploration of 2D superconducting properties and further applications in electrical devices.

Here, we demonstrate epitaxial CVD growth of 2D NbS$_2$ single crystals and continuous transition from a metallic 3R-polytype to superconducting 2H-polytype with respect to its thickness. Our NbS$_2$ flakes have a rectangular shape with a large grain size exceeding 500 μm and are highly aligned by quasi van der Waals epitaxy with an atomically smooth sapphire surface. The thickness can be tuned from 1.5 to 10 nm by changing the growth conditions. The thickness-dependent phase transition was clearly observed from Raman and STEM study, which is further confirmed by transport measurements for different phases, including the observation of superconductivity in layered 2H-NbS$_2$ below a transition temperature of 3 K.

RESULTS AND DISCUSSION

2D NbS$_2$ Grown by CVD. 2D NbS$_2$ was grown using a home-built CVD reactor schematically presented in Figure 1a. C-plane sapphire was used as the growth substrate and was annealed in air for 6 h prior to growth, resulting in a clean surface with atomically smooth step terraces,[25] which is crucial for achieving epitaxial growth.[26] A solution of niobium chloride (NbCl$_5$) was used as the precursor, while sodium chloride (NaCl) was used to reduce nucleation density[27] and the reaction energy barrier.[28] Both solvents were spin-coated on top of sapphire substrate before loading into the chamber. During the growth, as shown in Figure 1a, another bare sapphire wafer was placed on top of the spin-coated wafer. This promotes the growth of larger crystals by localizing the NbCl$_5$ vapor and reducing the flow rate of H$_2$S near the substrate.

We observe different morphologies of our CVD-grown NbS$_2$ crystals, depending on the growth parameters. Optical micro-graphs of CVD-grown NbS$_2$ crystals are shown in Figure 1b and Supplementary Figure S1. As can be seen from the figures, the shape and thickness of NbS$_2$ flakes show a clear trend, changing from thick triangles to thin rectangles with increasing temper-ature. It is notable that the rectangle-shaped NbS$_2$ flakes are grown with a large domain size having a typical length exceeding 500 μm and a width of around 40 μm, which is significantly larger than those in previous reports.[19,23,29] In addition, all the rectangular NbS$_2$ flakes are perfectly aligned in the same direction, confirmed by the orientation histogram shown in Supplementary Figure S2 for the same region as shown in Figure 1b. The single-crystalline structure was confirmed by selected area electron diffraction (SAED) patterns on several areas of an NbS$_2$ flake as shown in Supplementary Figure S3. The different crystal morphologies and the orientation of rectangular NbS$_2$ can be explained by the temperature-dependent strong interaction between NbS$_2$ and the sapphire substrate.[30] At the early stage of growth, nucleation takes place on the surface of
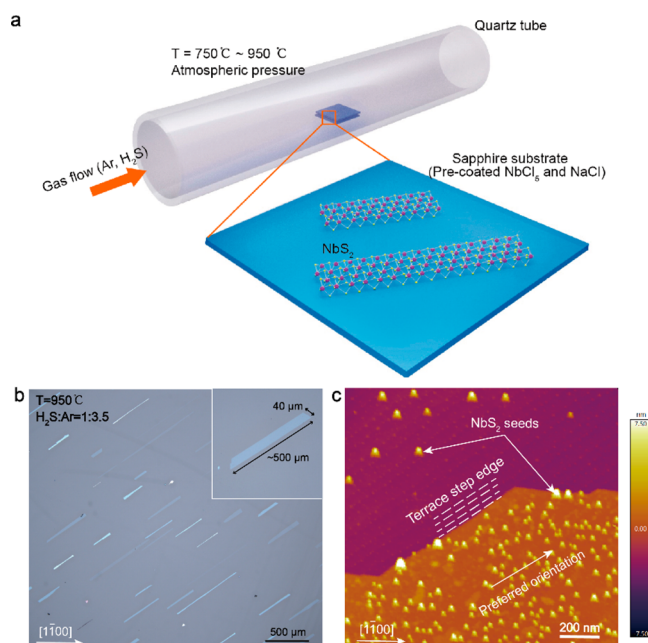

Figure 1. CVD growth of layered NbS$_2$ flakes. (a) Schematic illustration of the hot-wall CVD system for NbS$_2$ growth. In the chamber, a bare wafer was placed on top of the sapphire wafer, which was spin-coated with NaCl and NbCl$_5$ solutions. (b) Optical micrographs of as-grown NbS$_2$ flakes showing rectangular shapes and a large size exceeding 500 μm. The orientation of rectangular NbS$_2$ flakes is aligned in the same direction. (c) AFM image of the as-grown NbS$_2$ on a sapphire substrate, from an area shown in (b). NbS$_2$ seeds are epitaxially aligned along the $[1\bar{1}00]$ axis of c-plane sapphire, while the preferred growth orientation of rectangular NbS$_2$ flakes is determined by the terrace step edges.

sapphire with an initial random orientation of the crystallites.[31] For relatively low growth temperatures (e.g., 750 °C), the small crystallites do not have enough thermal energy to explore the energy landscape by rotation before they grow to big crystals. As a result, NbS$_2$ crystals with a small domain size and a random orientation are observed in Supplementary Figure S1a. We also observe a higher nucleation density under these conditions because of weak thermal etching. However, at higher growth temperatures (850 and 950 °C, Supplementary Figure S1b and Figure 1b), the orientation of the grown NbS$_2$ is determined by the underlying sapphire. This could be related to the orientation of step edges on the atomically smooth sapphire surface. An AFM image of rectangular NbS$_2$ crystals from the sample shown in Figure 1b is presented in Figure 1c, which clearly shows that the long edges of the NbS$_2$ crystal are oriented along the step edges on the surface of sapphire. In addition, we note that the smaller triangular NbS$_2$ crystals both on sapphire and on the NbS$_2$ thin film are epitaxially aligned along the $[1\bar{1}00]$ axis of the underlying c-plane sapphire (see Supplementary Figure S5), which can be explained by van der Waals interaction with the underlying substrate.[32]

Growth morphologies can also be modulated by the gas flow ratio of H$_2$S and Ar. Dendritic NbS$_2$ crystals were observed in Supplementary Figure S1c,d with a relatively lower value of H$_2$S:Ar compared with that in Figure 1b. The morphology transition induced by the gas flow ratio can be explained by the growth rates of different edge terminations.[33] In our case, the NbCl$_5$ precursor is reduced by H$_2$S and tiny NbS$_2$ seeds emerge at the early stage of growth. Along the edges of these tiny seeds,
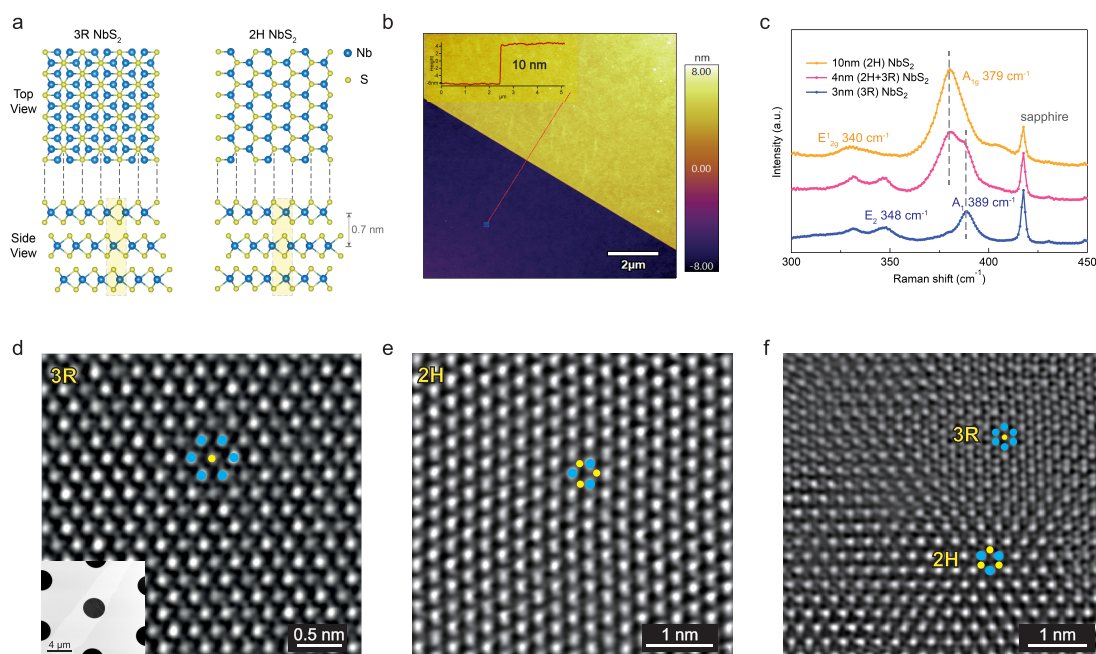
Figure 2. Phase transition of CVD-grown NbS$_2$ flakes. (a) Side and top views of atomic structures of NbS$_2$ with 3R-polytype stacking and 2H-polytype stacking. (b) AFM image of an NbS$_2$ flake transferred onto a Si/SiO$_2$ substrate. Inset shows the thickness of NbS$_2$ to be 10 nm. (c) Raman spectra at room temperature for as-grown NbS$_2$ flakes on sapphire substrate. The blue curve corresponds to the 3R-phase in 3 nm-thick NbS$_2$ flakes, and the orange curve shows the 2H-phase in 10 nm-thick NbS$_2$. The purple curve corresponds to a mixture of 2H and 3R phase in 4 nm-thick NbS$_2$. (d−f) STEM images of NbS$_2$ flakes with (d) 3R-polytype stacking, (e) 2H-polytype stacking and (f) a mixture of 3R-polytype stacking and 2H-polytype stacking. Inset of (d): A low magnification ADF-STEM image of a NbS$_2$ flake transferred onto a TEM grid.

Nb and S atoms are exposed to the reactor atmosphere on zigzag edges[33] with high chemical reactivity. They encounter atoms diffusing on the surface in random collisions and new chemical bonds are formed to achieve the most energetically stable structure.[34] Assuming that the spin-coated NbCl$_5$ provides the same amount of Nb precursor, the probability of meeting and bonding with free atoms depends on the partial pressure of H$_2$S. When the sulfur supply rate is at an insufficient level (e.g., H$_2$S: Ar = 1:8), S-terminated edges have much higher possibility to meet free Nb atoms, which leads to a higher growth rate of S-terminated edges than Nb-terminated edges. The difference in growth rates causes the dendritic shapes shown in Supplementary Figure S1c,d. As H$_2$S increases to a saturated level (e.g., H$_2$S: Ar = 1:3), both S- and Nb-terminated edges have enough opportunity to bond with free atoms, resulting in similar growth rates of these two types of edges. As a consequence, crystals grow with regular shapes and sharp edges as shown in Figure 1b.

Different Phases of CVD-Grown NbS$_2$. We find that our CVD-grown rectangular NbS$_2$ crystals can have both 3R and 2H-phase structures, depending on the thickness. Figure 2a illustrates the atomic structures of NbS$_2$ with 3R and 2H polytype stacking. Each layer is composed of a 1H single layer where the Nb atoms are coordinated in a trigonal prismatic shape, while adjacent layers interact via the van der Waals force and maintain the interlayer distance of around 0.7 nm.[29] The two polytypes are distinguished by relative rotation and atom alignment between the neighboring planes.[35] Atomic force microscopy (AFM), Raman spectroscopy and aberration-corrected STEM were further conducted to investigate the correlation between the phase transition and thickness.

Changing the NbCl$_5$ concentration allows us to control the thickness of rectangular NbS$_2$ crystals in the 1.5 to 10 nm range, corresponding to 2−14 layers. A histogram of the thickness

distribution of as-grown NbS$_2$ crystals for different pre-coated NbCl$_5$ concentrations is shown in Supplementary Figure S6, indicating that a higher NbCl$_5$ concentration leads to a higher dominant thickness. In Figure 2b, we show an AFM image of a rectangular NbS$_2$ single crystal with a thickness of 10 nm. A smooth surface and sharp edge can be clearly seen, indicating that our NbS$_2$ samples have a high crystallinity and good quality. Additional AFM images with various thicknesses ranging from 1.5 to 10 nm are shown in Supplementary Figure S7. Figure 2c shows the room-temperature Raman spectra acquired from as-grown rectangular NbS$_2$ crystals with various thicknesses on sapphire substrates. The blue curve presents the Raman spectrum from 3 nm-thick NbS$_2$ showing two characteristic peaks at 348 cm^{-1} (E$_2$) and 389 cm^{-1} (A$_1$), which corresponds to the 3R-phase NbS$_2$.[36] The orange curve, however, collected from 10 nm-thick NbS$_2$ is characterized by peaks located at 340 cm^{-1} (E$^1_{2g}$) and 379 cm^{-1} (A$_{1g}$), in agreement with the spectral signature of the 2H-phase NbS$_2$.[36] Data from the 4 nm-thick NbS$_2$ (purple curve) shows a mixture of Raman spectra for both 3R-phase and 2H-phase, indicating the transition between 2H and 3R occurs around this thickness.

The atomic structures of different phases and stackings can be directly visualized by employing aberration-corrected STEM. In Figure 2d−f, we show high-resolution high-angle annular dark-field (HAADF) STEM images obtained from transferred NbS$_2$ samples to distinguish different atomic structures and stacking arrangements with various thicknesses. The inset of Figure 2d shows a low-magnification HAADF image of a rectangular NbS$_2$ crystal transferred onto a TEM grid. The HAADF intensity is proportional to the square of the atomic number ($\sim$Z^2), allowing Nb and S atoms to be directly distinguished on the basis of the contrast of individual atomic columns. In Figure 2d, bright hexagonal rings (Nb atoms) with darker spots (S atoms) in the
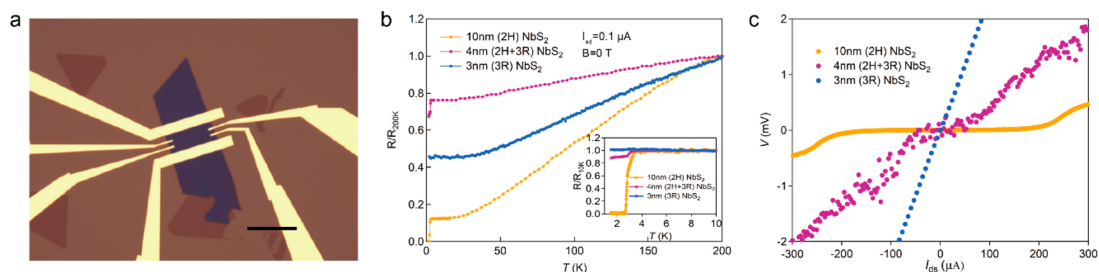
Figure 3. Transport properties of CVD-grown 2D NbS₂. (a) Optical micrograph of a NbS₂ device fabricated on Si/SiO₂ substrate with a flake thickness of 10 nm. Scale bar length: 25 μm. (b) Zero-field cooled resistance as a function of temperature for NbS₂ devices with different thicknesses. An AC current of 0.1 μA is used to probe the resistance. Inset: a zoomed-in temperature dependence of resistance from 1.4 K to 10 K. (c) $V-I$ characterization of NbS₂ devices with different thicknesses at the base temperature of 1.4 K.
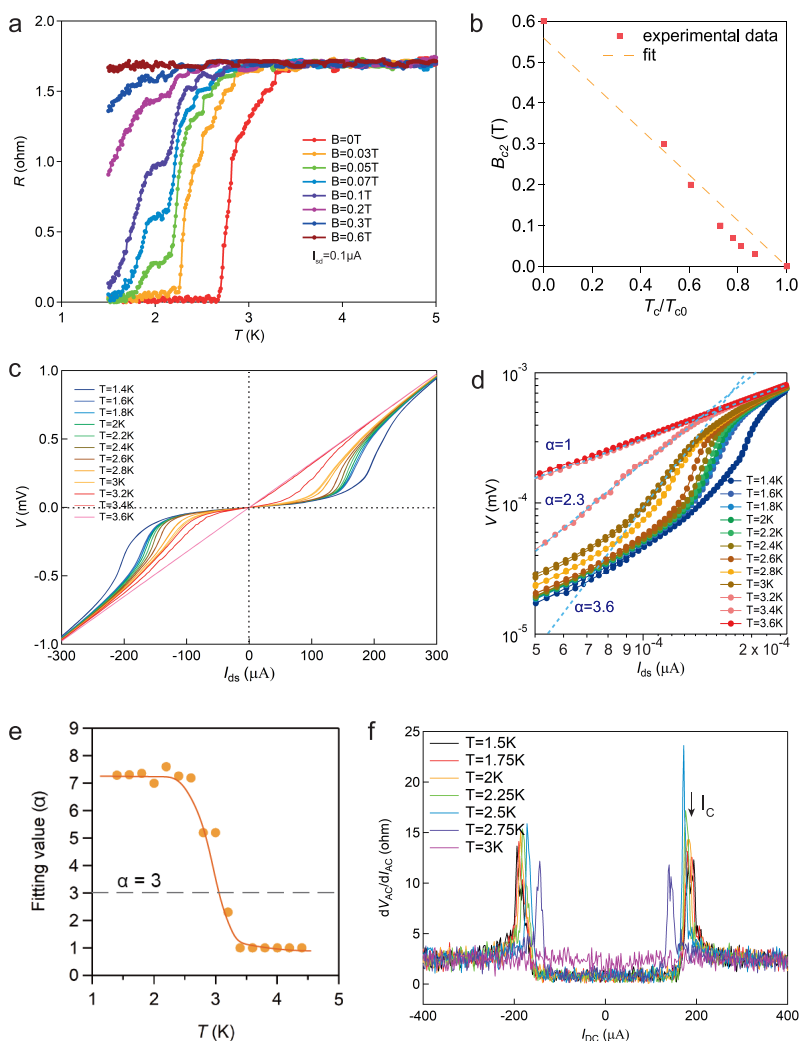

Figure 4. Superconductivity in 2H-phase NbS₂. (a) Electrical resistance of the device shown in Figure 3a at various out-of-plane magnetic fields B. (b) Corresponding B_{c2} vs T_c/T_{c0} diagram from the data shown in (a) with its fitting result. (c) $V-I$ characterization for 6 nm-thick NbS₂ device from the base temperature (1.4 K) to 3.6 K. (d) $V-I$ curve in (c) replotted on a logarithmic scale showing $V \propto I^\alpha$ behavior, consistent with an expected BKT model. (e) Fitting parameter α as a function of temperature from the data shown in (d). Gray dashed line corresponds to $\alpha = 3$, where the BKT transition temperature (T_{BKT}) is estimated to be 3 K for our 6 nm-thick NbS₂ flake. (f) Differential resistance at zero magnetic field as a function of source-drain bias current at different temperatures for the 6 nm-thick NbS₂ device.

center are displayed, indicating that the Nb atoms mismatch slightly without any rotation between adjacent layers (illustrated in Figure 2a), corresponding to a 3R-polytype stacking. On the other hand, an equal intensity of each Nb atom in Figure 2e reveals that they are aligned to each other with an opposite direction between adjacent layers (illustrated in Figure 2a) and

that 3 Nb atoms can be found around a single S atom, suggesting a 2H-polytype stacking. Additionally, a mixture of 3R and 2H polytype stacking is observed in Figure 2f. S line defects are visible close to the interfaces of different stackings, whereas S point defects are present everywhere in the image. A few of the defect positions are highlighted by yellow circles in the

corresponding filtered image in Supplementary Figure S9. Additionally, energy-dispersive X-ray spectrometry (EDX) and elemental mapping were also carried out on the transferred samples to confirm the chemical composition and material quality (see Supplementary Figure 10).

Electrical Transport in 2D NbS$_2$ with Different Phase Structures. In order to characterize the electrical transport properties of CVD-grown NbS$_2$ crystals with different phases, multiterminal devices were fabricated after the crystals have been transferred onto a Si/SiO$_2$ substrate. Figure 3a displays an optical micrograph of a Hall bar device based on a 10 nm-thick NbS$_2$ crystal. NbS$_2$ devices with various other thicknesses are shown in Supplementary Figure S11. The detailed fabrication process can be found in the Methods section.

To examine the relationship between the thickness-dependent structural phase and its transport properties, temperature dependence of four-probe longitudinal resistance (R_{xx}) was measured at zero magnetic field and the results for three representative thicknesses (3, 4, and 10 nm) shown in Figure 3b. The inset shows the magnified view in the 1.5−10 K temperature range. For the sample with a thickness of 3 nm (blue curve), the resistance linearly decreases as the temperature is lowered, indicating its metallic property ($dR/dT > 0$), which is consistent with previous predictions.[37] However, its resistance starts to slightly increase below 20 K, where the resistance minimum is observed (see Supplementary Figure S12). Similar observations of this low-temperature resistance minimum were reported in CVD-grown 3R-phase NbS$_2$,[19,29] which is attributed to electron scattering at defect or excess Nb sites. From the device, we do not observe the superconducting transition above our experimental base temperature (1.4 K). These electrical properties agree well with the metallic nature of the 3R-phase NbS$_2$. On the other hand, for the 2H-phase sample with a thickness of 10 nm (shown as orange curve), the resistance drops sharply to zero at around 3 K, indicating the superconducting transition. The superconducting transition critical temperature T_c is 2.6 K, which corresponds to the temperature at which the resistance becomes half of the normal-state resistance (R_N), $R(T_c) = 0.5 R_N$. At the intermediate thickness (4 nm) between the 2H and 3R phase of NbS$_2$ (shown as the purple curve), interestingly, the resistance drops sharply at around 3 K but remains at a relatively high value (~150 Ω) down to the base temperature of 1.4 K. This feature could be explained by the presence of mixed 2H and 3R phases where metallic 3R-phase and superconducting 2H-phase domains coexist. Magnetic field cooling suppresses this sharp resistance drop (shown in Supplementary Figure S13), which further supports the hypothesis that the resistance drop is related to the superconducting transition of the 2H domains. Notably, this 4 nm-thick device shows metallic behavior at high temperatures but with a slower resistance change (dR/dT) than that of the other 2H and 3R devices. This leads to a low residual resistance ratio (RRR) of ~1.5, defined as the ratio between the resistance at $T = 300$ K and the normal-state resistance above the superconducting transition temperature of the 2H phase, at $T = 10$ K, which is lower than that of the 3 nm-thick 3R-phase (~3.3) and 10 nm-thick 2H phase (~11). Since RRR is commonly used as an indicator of the crystalline quality of a superconductor,[38,39] a smaller RRR in 4 nm-thick NbS$_2$ indicates the existence of additional structural disorder, which we attribute to sulfur point and line defects between 2H and 3R phases, as confirmed by the STEM results shown in Supplementary Figure S9. Figure 3c displays four-probe DC $V−I$ characteristics for NbS$_2$ with

different structural phase at the base temperature (1.4 K). A linear curve was obtained for the 3 nm-thick 3R-phase NbS$_2$ sample, whereas a strong nonlinear curve was obtained for the 10 nm-thick 2H-phase NbS$_2$, consistent with a Berezinskii−Kosterlitz−Thouless (BKT) type superconducting phase transition. Compared with single-phase samples, the $V−I$ curve of the 4 nm-thick sample shows a weak nonlinear curve (a possible combination of 2H and 3R-phase signals) but with a larger noise, which could be related to contributions from line defects separating the two phases. These results, consistent with Raman and STEM results, provide additional evidence that transition from the metallic 3R-polytype to the superconducting 2H-polytype takes place in our thickness-controlled CVD-grown NbS$_2$ crystals.

Superconductivity of 2H-Phase NbS$_2$. To further study the superconductivity of CVD-grown 2H-phase NbS$_2$ crystals, both four-probe DC and AC transport measurements were performed. Figure 4a shows the temperature dependence of resistance (R_{xx}) of the device shown in Figure 3a at various out-of-plane external magnetic fields B, applied perpendicularly to the 2D crystal plane. In the presence of the magnetic field, we define the critical temperature T_c as the temperature at which the resistance decreases to 80% of the normal-state resistance value. As the amplitude of the magnetic field increases, the critical transition temperature decreases and the resistance change becomes more gradual. A metallic behavior without resistance drop was obtained above the magnetic field of 0.6 T, indicating that superconductivity is completely suppressed by the magnetic field. Figure 4b shows the magnetic field-dependent transition, B_{c2} vs T_c/T_{c0} phase diagram where H_{c2} is the upper critical field and T_{c0} the critical temperature at zero magnetic field. We find a linear relation between H_{c2} and T_c, which is a typical feature of 2D superconductors.[40,41] It can be fitted with a model from the linearized Ginzburg−Landau (GL) theory,[42] $B_{c2}(T) = \frac{\phi_0}{2\pi\xi_{GL}(0)^2}\left(1 - \frac{T_c}{T_{c0}}\right)$, where $\xi_{GL}(0)$ is zero-temperature coherence length, and ϕ_0 is magnetic flux quantum. From the fitted result, we get $\xi_{GL}(0) = 25$ nm, which is larger than the probed sample thickness (10 nm). This indicates that the 2D superconducting transition should follow the BKT type transition. Figure 4c shows the four-probe DC $I−V$ characteristics as a function of temperature for the 6 nm-thick 2H-phase NbS$_2$ device. At 3.5 K, linear Ohmic behavior was obtained with the constant slope of resistance around 3 Ω, which is equal to the metallic normal-state resistance (shown in Supplementary Figure S14). As the temperature decreases, the curve becomes nonlinear and a critical current gap is observed at which the probe voltage is close to zero. The $V−I$ curves plotted on a logarithmic scale (shown in Figure 4d) display a clear transition from a $V−I$ linear dependence to a power-law dependence ($V \propto I^\alpha$) indicating the BKT transition. We estimate the BKT transition temperature (T_{BKT}) to be 3 K at the value of $\alpha = 3$ for our 6 nm-thick NbS$_2$ crystal. Fitted α values as a function of temperature can be found in Figure 4e. The data presented above provides further evidence that our CVD-grown 2H-phase NbS$_2$ exhibits the features expected from a 2D superconductor.

To further investigate the superconducting critical current, AC differential resistance as a function of DC drain-source current was measured at fixed temperatures ranging from 1.5 to 3 K as shown in Figure 4f. Resistance peaks sharply at the critical current (190 μA at 1.5 K), which indicates the transition from the normal resistive state to the superconducting zero-resistance state. The critical current gradually decreases with an increasing

temperature and disappears above 3 K as the sample becomes metallic.

CONCLUSIONS

We demonstrate a CVD method to synthesize 2D NbS_2 single crystals with a large size, controllable thickness, and epitaxial orientation. The thickness-dependent structural transition from metallic 3R-phase to superconducting 2H-phase was first observed in CVD-grown NbS_2 and was confirmed by Raman spectroscopy, aberration-corrected STEM as well as transport measurements. The CVD-grown 2H-phase NbS_2 behaves as a 2D superconductor, with BKT-type superconducting transition occurring below 3 K. Our work demonstrates a practical approach to phase-controllable growth of 2D TMDC superconductors for their widespread use in mesoscopic devices.

METHODS

Material Synthesis. Rectangular NbS_2 single crystals were synthesized using chemical vapor deposition (CVD) method in the home-built system schematically represented in Figure 1a. Before growth, c-plane sapphire wafers were annealed in air for 6 h and spin-coated with 0.3 mol/L NaCl solution in deionized water as well as $NbCl_5$ solution in isopropanol (IPA). Afterward, a sapphire wafer was loaded into the quartz chamber and covered with another bare sapphire wafer. Prior to growth, the reactor tube was purged with argon to remove residual oxygen and humidity. During the whole growth process, hydrogen disulfide (H_2S) with a flow rate of 35 sccm was delivered to the chamber by using argon as a carrier gas. The growth procedure lasts for 30 min at the temperature of 950 °C and atmospheric pressure. As soon as the growth is finished, the chamber is allowed to cool down naturally. H_2S flow was kept with a flow rate of 5 sccm until the furnace reached the temperature of 150 °C to reduce sulfur vacancies.

Raman Spectroscopy. Raman spectra of the NbS_2 flakes were performed on as-grown samples on sapphire substrates. A spectrometer (Renishaw inVia Confocal Raman Microscope) was utilized to collect the spectrum with a 532 nm laser and a grating of 3000 g/mm at room temperature. The excitation spot size is around 1 μm with a power of 1 mW.

Scanning Transmission Electron Microscopy Measurements. The as-grown samples were spin-coated with PMMA (poly(methyl methacrylate)) A4 at a speed of 2000 rpm for 60 s and heated on a hot plate for drying at 180 °C for 5 min. After immerging in water for 5 min, the PMMA film together with NbS_2 samples was detached by water tension and picked up using a silicon nitride TEM grid. Subsequently, the samples were baked on a hot plate for drying and promoting the adhesion at 65 °C for 10 min. Finally, the PMMA film was removed by immersing in acetone overnight followed by annealing in high vacuum at 250 °C for 6 h.

High-resolution high-angle annular dark filed (HAADF) STEM imaging was performed using a double aberration-corrected FEI Titan Themis, which is equipped with a X-FEG, Super-X EDX detector, and monochromator. The beam convergence half angle was set to 20 mrad which corresponds to the HAADF detector 49.5−198 mrad collection angle. The microscope was operated at an accelerating voltage of 80 kV, which is below the electron-beam induced knock-on damage of NbS_2. The electron probe current was set to ~20 pA. To avoid the sample drift, images were acquired at various places using a raster scan with 512 × 512 pixels and 8 μs dwell times. EDX measurements were performed in both Titan Themis and FEI Talos TEM. EDX spectrum and elemental mapping were processed in Velox software, ThermoFisher Scientific. Inverse fast Fourier transform filtering has been applied to magnified images to enhance the contrast and highlight the atomic structures of different phases.

Sample Transfer and Device Fabrication. The as-grown NbS_2 flakes were transferred from sapphire to SiO_2/Si substrate by using the same method as for the preparation of TEM samples. Afterward, the samples were spin-coated with PMMA polymer and put on a hot plate

at 180 °C for 5 min. Electron-beam lithography was used to pattern the electrodes. Finally, a stack of 2 nm/80 nm thick Ti/Au was deposited by e-beam evaporation for the electrodes, followed with a lift-off process with acetone to remove the PMMA layer. Between the fabrication steps, samples were kept in the inert Ar environment inside a glovebox to prevent sample degradation in air.

Transport Measurements. Cryogenic electrical transport measurements were performed in ICE Oxford liquid helium continuous flow system with the base temperature of ~1.4 K. Temperature dependent four-probe longitudinal resistance (R_{xx}) were measured using SR860 lock-in amplifier with an AC probe current I_{ac} = 100 nA at 13.3 Hz. DC voltage−current ($V-I$) characteristics was measured by applying constant DC current with Keithley 2636b sourcemeter while measuring DC voltage with Keithley 2182a nanovoltmeter. Four-probe differential resistance (dV_{ac}/dI_{ac}) was measured using the lock-in amplifier with AC probe current I_{ac} = 100 nA at 13.3 Hz while sweeping the DC current.

ASSOCIATED CONTENT

Supporting Information

The Supporting Information is available free of charge at https://pubs.acs.org/doi/10.1021/acsnano.1c07956.

Optical micrographs under different growth condition; histogram of orientation distribution; selected area electron diffraction; large-scale TEM images; AFM images from different areas; histogram of thickness distribution with various $NbCl_5$ concentrations; AFM images with various thicknesses; TEM images of hexagonal NbS_2 flake; EDX analysis; STEM images showing a mixture of 3R and 2H phase; optical micrographs of NbS_2 devices; temperature dependent resistance of NbS_2 devices (PDF)

The data that support the findings of this study are available in Zenodo at http://dx.doi.org/10.5281/zenodo.5645160.

AUTHOR INFORMATION

Corresponding Author

Andras Kis − *Institute of Electrical and Microengineering, École Polytechnique Fédérale de Lausanne (EPFL), CH-1015 Lausanne, Switzerland; Institute of Materials Science and Engineering, École Polytechnique Fédérale de Lausanne (EPFL), CH-1015 Lausanne, Switzerland;* orcid.org/0000-0002-3426-7702; Email: andras.kis@epfl.ch

Authors

Zhenyu Wang − *Institute of Electrical and Microengineering, École Polytechnique Fédérale de Lausanne (EPFL), CH-1015 Lausanne, Switzerland; Institute of Materials Science and Engineering, École Polytechnique Fédérale de Lausanne (EPFL), CH-1015 Lausanne, Switzerland*

Cheol-Yeon Cheon − *Institute of Electrical and Microengineering, École Polytechnique Fédérale de Lausanne (EPFL), CH-1015 Lausanne, Switzerland; Institute of Materials Science and Engineering, École Polytechnique Fédérale de Lausanne (EPFL), CH-1015 Lausanne, Switzerland*

Mukesh Tripathi − *Institute of Electrical and Microengineering, École Polytechnique Fédérale de Lausanne (EPFL), CH-1015 Lausanne, Switzerland; Institute of Materials Science and Engineering, École Polytechnique Fédérale de Lausanne (EPFL), CH-1015 Lausanne, Switzerland*

Guilherme Migliato Marega − *Institute of Electrical and Microengineering, École Polytechnique Fédérale de Lausanne (EPFL), CH-1015 Lausanne, Switzerland; Institute of*

Materials Science and Engineering, École Polytechnique Fédérale de Lausanne (EPFL), CH-1015 Lausanne, Switzerland

Yanfei Zhao − Institute of Electrical and Microengineering, École Polytechnique Fédérale de Lausanne (EPFL), CH-1015 Lausanne, Switzerland; Institute of Materials Science and Engineering, École Polytechnique Fédérale de Lausanne (EPFL), CH-1015 Lausanne, Switzerland

Hyun Goo Ji − Institute of Electrical and Microengineering, École Polytechnique Fédérale de Lausanne (EPFL), CH-1015 Lausanne, Switzerland; Institute of Materials Science and Engineering, École Polytechnique Fédérale de Lausanne (EPFL), CH-1015 Lausanne, Switzerland

Michal Macha − Institute of Bioengineering, École Polytechnique Fédérale de Lausanne (EPFL), CH-1015 Lausanne, Switzerland

Aleksandra Radenovic − Institute of Bioengineering, École Polytechnique Fédérale de Lausanne (EPFL), CH-1015 Lausanne, Switzerland; ⊙ orcid.org/0000-0001-8194-2785

Complete contact information is available at:
https://pubs.acs.org/10.1021/acsnano.1c07956

Author Contributions

[⊥](Z.W., C.-Y.C.) These authors contributed equally

Author Contributions

A.K. initiated and supervised the work. Z.W. performed the CVD growth of NbS₂ flakes with initial assistance of Y.Z. Z.W. and M.M. improved the CVD system with supervision of A.R. Z.W. fabricated the devices with initial assistance of G.M.M. C.-Y.C. and Z.W. designed and performed electrical measurements. M.T. performed STEM measurements and EDX spectroscopy. Z.W. performed AFM and Raman spectroscopy with help of H.G.J. A.K., Z.W., and C.-Y.C. analyzed the data with input from M.T. and H.J. All the authors contributed to the writing of the manuscript.

Notes

The authors declare no competing financial interest.

REFERENCES

(1) Splendiani, A.; Sun, L.; Zhang, Y.; Li, T.; Kim, J.; Chim, C.-Y.; Galli, G.; Wang, F. Emerging Photoluminescence in Monolayer MoS₂. *Nano Lett.* **2010**, *10* (4), 1271−1275.

(2) Radisavljevic, B.; Radenovic, A.; Brivio, J.; Giacometti, V.; Kis, A. Single-Layer MoS₂ Transistors. *Nat. Nanotechnol.* **2011**, *6* (3), 147−150.

(3) Unuchek, D.; Ciarrocchi, A.; Avsar, A.; Watanabe, K.; Taniguchi, T.; Kis, A. Room-Temperature Electrical Control of Exciton Flux in a van der Waals Heterostructure. *Nature* **2018**, *560* (7718), 340−344.

(4) Allain, A.; Kang, J.; Banerjee, K.; Kis, A. Electrical Contacts to Two-Dimensional Semiconductors. *Nat. Mater.* **2015**, *14* (12), 1195−1205.

(5) Ding, X.; Zhang, S.; Zhao, M.; Xiang, Y.; Zhang, K. H. L.; Zu, X.; Li, S.; Qiao, L. NbS₂: A Promising *p*-Type Ohmic Contact for Two-Dimensional Materials. *Phys. Rev. Appl.* **2019**, *12* (6), 064061.

(6) Liu, Y.; Stradins, P.; Wei, S.-H. Van Der Waals Metal-Semiconductor Junction: Weak Fermi Level Pinning Enables Effective Tuning of Schottky Barrier. *Science Advances* **2016**, *2* (4), e1600069.

(7) Geim, A. K.; Grigorieva, I. V. Van der Waals Heterostructures. *Nature* **2013**, *499* (7459), 419−425.

(8) Guillamón, I.; Suderow, H.; Vieira, S.; Cario, L.; Diener, P.; Rodière, P. Superconducting Density of States and Vortex Cores of 2H-NbS₂. *Phys. Rev. Lett.* **2008**, *101* (16), 166407.

(9) Yokoya, T.; Kiss, T.; Chainani, A.; Shin, S.; Nohara, M.; Takagi, H. Fermi Surface Sheet-Dependent Superconductivity in 2H-NbSe₂. *Science* **2001**, *294* (5551), 2518−2520.

(10) Zhu, X.; Guo, Y.; Cheng, H.; Dai, J.; An, X.; Zhao, J.; Tian, K.; Wei, S.; Cheng Zeng, X.; Wu, C.; Xie, Y. Signature of Coexistence of Superconductivity and Ferromagnetism in Two-Dimensional NbSe₂ Triggered by Surface Molecular Adsorption. *Nat. Commun.* **2016**, *7* (1), 11210.

(11) Chatterjee, U.; Zhao, J.; Iavarone, M.; Di Capua, R.; Castellan, J. P.; Karapetrov, G.; Malliakas, C. D.; Kanatzidis, M. G.; Claus, H.; Ruff, J. P. C.; Weber, F.; van Wezel, J.; Campuzano, J. C.; Osborn, R.; Randeria, M.; Trivedi, N.; Norman, M. R.; Rosenkranz, S. Emergence of Coherence in the Charge-Density Wave State of 2H -NbSe₂. *Nat. Commun.* **2015**, *6* (1), 6313.

(12) Leroux, M.; Cario, L.; Bosak, A.; Rodière, P. Traces of Charge Density Waves in NbS₂. *Phys. Rev. B: Condens. Matter Mater. Phys.* **2018**, *97* (19), 195140.

(13) Majumdar, A.; VanGennep, D.; Brisbois, J.; Chareev, D.; Sadakov, A. V.; Usoltsev, A. S.; Mito, M.; Silhanek, A. V.; Sarkar, T.; Hassan, A.; Karis, O.; Ahuja, R.; Abdel-Hafiez, M. Interplay of Charge Density Wave and Multiband Superconductivity in Layered Quasi-Two-Dimensional Materials: The Case of NbS₂ and NbSe₂. *Phys. Rev. Materials* **2020**, *4* (8), 084005.

(14) Lv, P.; Zhou, Y.-F.; Yang, N.-X.; Sun, Q.-F. Magnetoanisotropic Spin-Triplet Andreev Reflection in Ferromagnet-Ising Superconductor Junctions. *Phys. Rev. B: Condens. Matter Mater. Phys.* **2018**, *97* (14), 144501.

(15) Dvir, T.; Zalic, A.; Fyhn, E. H.; Amundsen, M.; Taniguchi, T.; Watanabe, K.; Linder, J.; Steinberg, H. Planar Graphene-NbSe₂ Josephson Junctions in a Parallel Magnetic Field. *Phys. Rev. B: Condens. Matter Mater. Phys.* **2021**, *103* (11), 115401.

(16) Bianco, R.; Errea, I.; Monacelli, L.; Calandra, M.; Mauri, F. Quantum Enhancement of Charge Density Wave in NbS₂ in the Two-Dimensional Limit. *Nano Lett.* **2019**, *19* (5), 3098−3103.

(17) Güller, F.; Vildosola, V. L.; Llois, A. M. Spin Density Wave Instabilities in the NbS₂ Monolayer. *Phys. Rev. B: Condens. Matter Mater. Phys.* **2016**, *93* (9), 094434.

(18) van Loon, E. G. C. P.; Rösner, M.; Schönhoff, G.; Katsnelson, M. I.; Wehling, T. O. Competing Coulomb and Electron−Phonon Interactions in NbS₂. *npj Quant Mater.* **2018**, *3* (1), 1−8.

(19) Zhao, S.; Hotta, T.; Koretsune, T.; Watanabe, K.; Taniguchi, T.; Sugawara, K.; Takahashi, T.; Shinohara, H.; Kitaura, R. Two-Dimensional Metallic NbS₂: Growth, Optical Identification and Transport Properties. *2D Mater.* **2016**, *3* (2), 025027.

(20) Fisher, W. G.; Sienko, M. J. Stoichiometry, Structure, and Physical Properties of Niobium Disulfide. *Inorg. Chem.* **1980**, *19* (1), 39−43.

(21) Izawa, K.; Ida, S.; Unal, U.; Yamaguchi, T.; Kang, J.-H.; Choy, J.-H.; Matsumoto, Y. A New Approach for the Synthesis of Layered Niobium Sulfide and Restacking Route of NbS₂ Nanosheet. *J. Solid State Chem.* **2008**, *181* (2), 319−324.

(22) Benameur, M. M.; Radisavljevic, B.; Heron, J. S.; Sahoo, S.; Berger, H.; Kis, A. Visibility of Dichalcogenide Nanolayers. *Nanotechnology* **2011**, *22* (12), 125706.

(23) Zhang, Y.; Yin, L.; Chu, J.; Shifa, T. A.; Xia, J.; Wang, F.; Wen, Y.; Zhan, X.; Wang, Z.; He, J. Edge-Epitaxial Growth of 2D NbS$_2$-WS$_2$ Lateral Metal-Semiconductor Heterostructures. *Adv. Mater.* **2018**, *30* (40), 1803665.

(24) Kozhakhmetov, A.; Choudhury, T. H.; Al Balushi, Z. Y.; Chubarov, M.; Redwing, J. M. Effect of Substrate on the Growth and Properties of Thin 3R NbS$_2$ Films Grown by Chemical Vapor Deposition. *J. Cryst. Growth* **2018**, *486*, 137−141.

(25) Yoshimoto, M.; Maeda, T.; Ohnishi, T.; Koinuma, H.; Ishiyama, O.; Shinohara, M.; Kubo, M.; Miura, R.; Miyamoto, A. Atomic-Scale Formation of Ultrasmooth Surfaces on Sapphire Substrates for High-quality Thin-film Fabrication. *Appl. Phys. Lett.* **1995**, *67* (18), 2615−2617.

(26) Dumcenco, D.; Ovchinnikov, D.; Marinov, K.; Lazić, P.; Gibertini, M.; Marzari, N.; Sanchez, O. L.; Kung, Y.-C.; Krasnozhon, D.; Chen, M.-W.; Bertolazzi, S.; Gillet, P.; Fontcuberta i Morral, A.; Radenovic, A.; Kis, A. Large-Area Epitaxial Monolayer MoS$_2$. *ACS Nano* **2015**, *9* (4), 4611−4620.

(27) Kim, H.; Ovchinnikov, D.; Deiana, D.; Unuchek, D.; Kis, A. Suppressing Nucleation in Metal−Organic Chemical Vapor Deposition of MoS$_2$ Monolayers by Alkali Metal Halides. *Nano Lett.* **2017**, *17* (8), 5056−5063.

(28) Yang, P.; Zou, X.; Zhang, Z.; Hong, M.; Shi, J.; Chen, S.; Shu, J.; Zhao, L.; Jiang, S.; Zhou, X.; Huan, Y.; Xie, C.; Gao, P.; Chen, Q.; Zhang, Q.; Liu, Z.; Zhang, Y. Batch Production of 6-Inch Uniform Monolayer Molybdenum Disulfide Catalyzed by Sodium in Glass. *Nat. Commun.* **2018**, *9* (1), 979.

(29) Wang, X.; Lin, J.; Zhu, Y.; Luo, C.; Suenaga, K.; Cai, C.; Xie, L. Chemical Vapor Deposition of Trigonal Prismatic NbS$_2$ Monolayers and 3R-Polytype Few-Layers. *Nanoscale* **2017**, *9* (43), 16607−16611.

(30) Song, G.; Remhof, A.; Theis-Bröhl, K.; Zabel, H. Extraordinary Adhesion of Niobium on Sapphire Substrates. *Phys. Rev. Lett.* **1997**, *79* (25), 5062−5065.

(31) Ma, Z.; Wang, S.; Deng, Q.; Hou, Z.; Zhou, X.; Li, X.; Cui, F.; Si, H.; Zhai, T.; Xu, H. Epitaxial Growth of Rectangle Shape MoS$_2$ with Highly Aligned Orientation on Twofold Symmetry a-Plane Sapphire. *Small* **2020**, *16* (16), 2000596.

(32) Ago, H.; Fukamachi, S.; Endo, H.; Solís-Fernández, P.; Mohamad Yunus, R.; Uchida, Y.; Panchal, V.; Kazakova, O.; Tsuji, M. Visualization of Grain Structure and Boundaries of Polycrystalline Graphene and Two-Dimensional Materials by Epitaxial Growth of Transition Metal Dichalcogenides. *ACS Nano* **2016**, *10* (3), 3233−3240.

(33) Wang, S.; Rong, Y.; Fan, Y.; Pacios, M.; Bhaskaran, H.; He, K.; Warner, J. H. Shape Evolution of Monolayer MoS$_2$ Crystals Grown by Chemical Vapor Deposition. *Chem. Mater.* **2014**, *26* (22), 6371−6379.

(34) Ataca, C.; Şahin, H.; Ciraci, S. Stable, Single-Layer MX$_2$ Transition-Metal Oxides and Dichalcogenides in a Honeycomb-Like Structure. *J. Phys. Chem. C* **2012**, *116* (16), 8983−8999.

(35) Shi, J.; Yu, P.; Liu, F.; He, P.; Wang, R.; Qin, L.; Zhou, J.; Li, X.; Zhou, J.; Sui, X.; Zhang, S.; Zhang, Y.; Zhang, Q.; Sum, T. C.; Qiu, X.; Liu, Z.; Liu, X. 3R MoS$_2$ with Broken Inversion Symmetry: A Promising Ultrathin Nonlinear Optical Device. *Adv. Mater.* **2017**, *29* (30), 1701486.

(36) McMullan, W. G.; Irwin, J. C. Raman Scattering from 2H and 3R−NbS$_2$. *Solid State Commun.* **1983**, *45* (7), 557−560.

(37) Kuc, A.; Zibouche, N.; Heine, T. Influence of Quantum Confinement on the Electronic Structure of the Transition Metal Sulfide TS$_2$. *Phys. Rev. B: Condens. Matter Mater. Phys.* **2011**, *83* (24), 245213.

(38) Wang, H.; Huang, X.; Lin, J.; Cui, J.; Chen, Y.; Zhu, C.; Liu, F.; Zeng, Q.; Zhou, J.; Yu, P.; Wang, X.; He, H.; Tsang, S. H.; Gao, W.; Suenaga, K.; Ma, F.; Yang, C.; Lu, L.; Yu, T.; Teo, E. H. T.; et al. High-Quality Monolayer Superconductor NbSe$_2$ Grown by Chemical Vapour Deposition. *Nat. Commun.* **2017**, *8* (1), 394.

(39) Li, J.; Song, P.; Zhao, J.; Vaklinova, K.; Zhao, X.; Li, Z.; Qiu, Z.; Wang, Z.; Lin, L.; Zhao, M.; Herng, T. S.; Zuo, Y.; Jonhson, W.; Yu, W.; Hai, X.; Lyu, P.; Xu, H.; Yang, H.; Chen, C.; Pennycook, S. J.; et al. Printable Two-Dimensional Superconducting Monolayers. *Nat. Mater.* **2021**, *20* (2), 181−187.

(40) Xi, X.; Wang, Z.; Zhao, W.; Park, J.-H.; Law, K. T.; Berger, H.; Forró, L.; Shan, J.; Mak, K. F. Ising Pairing in Superconducting NbSe$_2$ Atomic Layers. *Nat. Phys.* **2016**, *12* (2), 139−143.

(41) Xu, C.; Wang, L.; Liu, Z.; Chen, L.; Guo, J.; Kang, N.; Ma, X.-L.; Cheng, H.-M.; Ren, W. Large-Area High-Quality 2D Ultrathin Mo$_2$C Superconducting Crystals. *Nat. Mater.* **2015**, *14* (11), 1135−1141.

(42) Tsen, A. W.; Hunt, B.; Kim, Y. D.; Yuan, Z. J.; Jia, S.; Cava, R. J.; Hone, J.; Kim, P.; Dean, C. R.; Pasupathy, A. N. Nature of the Quantum Metal in a Two-Dimensional Crystalline Superconductor. *Nat. Phys.* **2016**, *12* (3), 208−212.

(43) Momma, K.; Izumi, F. VESTA 3 for Three-Dimensional Visualization of Crystal, Volumetric and Morphology Data. *J. Appl. Crystallogr.* **2011**, *44* (6), 1272−1276.